This is the accepted version of the following article: Xie XX, Zhang LX, Qu Z*. A critical review of methods for determining the damage states for the in-plane fragility of masonry infill walls. ***Journal of Earthquake Engineering***. This article may be used for non-commercial purposes.

A critical review of methods for determining the damage states for the in-plane fragility of masonry infill walls

We subjected nine full-scale masonry infilled reinforced concrete frame specimens to quasi-static cyclic loading to critically review the methods for determining the damage state of masonry infill walls to develop reliable in-plane fragility functions. Among the three methods, the method based on maximum crack widths gave the smallest dispersion, whereas the skeleton curve-based methods generated excessive dispersions and the phenomena-based method was shown to be self-contradictory in certain circumstances. If the damage states were determined by maximum crack widths, neither the brick type nor the plaster had a significant influence on the fragility functions.

Keywords: fragility function; damage state; crack width; hollow concrete block; solid clay brick

Introduction

Masonry infill walls are among the most employed internal partitions and external enclosures in reinforced concrete (RC) and steel frame buildings in many earthquake-prone regions in the world, such as Europe, China, and part of the US. Although classified as nonstructural components, masonry infill walls have been recognized as having a non-negligible influence on the seismic performance of frame structures (Mainstone 1971; Paulay and Priestley 1992). Extensive experimental efforts have been made to study both the detrimental impacts, such as the shear failure of captive columns (Mehrabi et al. 1996) and unintended structural irregularity (Negro and Colombo 1997; Verderame et al. 2011), and the beneficial effects of increasing the stiffness, strength, and energy dissipation of a structure (Calvi et al. 2004; Pujol et al. 2008).

In addition to the influence on the structural behavior, masonry infill walls are a major source of nonstructural damage to buildings in moderate and major earthquakes, which has attracted increasing attentions since the 1990s when performance-based earthquake engineering (PBEE) became a mainstream (Holmes 2000). Compared with the surrounding frames, masonry infill walls are usually stiff but weak, and thus are vulnerable to extensive damage at small lateral drifts when the structure remains essentially elastic. In the 2013 M7.0 Lushan earthquake in China, masonry infill walls of either hollow blocks or solid bricks sustained extensive damage, while the structural failure in the same earthquake was limited (Yan et al. 2014).

Considering not only their previously mentioned high fragility but also the considerable cost (Taghavi and Miranda 2003), masonry infill walls are essential for the seismic loss assessments of buildings, which are in a probabilistic format in the PBEE framework and require the establishment of fragility functions of various types of structural and nonstructural components. A fragility function describes the probability of

experiencing or exceeding a prescribed damage state (DS) conditioned on a chosen intensity measure (*IM*). For a specific class of components, the damage states are usually discrete because they are associated with consequence functions and the consequences such as the loss of a component or unit repair cost are discrete. The *IM* is a physically determinant quantity that is strongly correlated with the extents of damage to the components. A reasonable choice of *IM* would help reduce the unwarranted uncertainty in the fragility function (Porter et al 2007).

In contrast to the many experimental tests on masonry infilled frames that focus on the structural performance, few experimental efforts have been made with a focus on the seismic fragility of masonry infill walls. Cardone and Perrone (2015) collected 55 specimens from 19 studies to form several samples for developing fragility functions of masonry infill walls at four DSs from light cracking to collapse. The story drift ratio and peak floor acceleration were selected as the *IM*s for the in-plane fragility functions and out-of-plane fragility functions, respectively. Similarly, Sassun et al. (2016) developed a set of in-plane fragility functions at four damage states of masonry infill walls based on a sample of 50 specimens extracted from 14 studies. In addition to the story drift ratio as an *IM*, they defined an apparent strain of the equivalent diagonal strut for the *IM*, only to conclude that the fragility functions based on the two *IM*s were not significantly different in terms of dispersions. It suggested a weak influence of the aspect ratio on the in-plane fragility of masonry walls. Their results also showed that the brick type had a significant influence on the fragility. Chiozzi and Miranda (2017) built a larger-than-ever-before database of 152 specimens of various parameters, such as the brick type, dimensions, and presence of openings, to develop a family of fragility functions with the story drift ratio as the *IM*. A comprehensive statistical analysis was performed to show that the brick type was not statistically significant for all DSs, which was an opposite conclusion to that obtained by Sassun et al. (2016). They also discovered that the prism strength, mortar strength and the presence of openings were statistically significant for the fragility functions of masonry walls.

The efforts of establishing databases of existing experimental results for masonry infilled frames are important for providing an empirical basis for the development of reliable fragility functions of masonry infill walls. However, difficulties may have occurred in determining the DSs based on the existing test results because most of the tests in the literature focused on the structural responses, and thus, the descriptions of the damage to the masonry walls were not always adequate. More importantly, the descriptions could be subjective, ambiguous, and even inconsistent from test to test, which left the determination of the onset of a DS to the judgment of the researchers who processed the data. The lack of quantitative data on the damage to masonry walls and the corresponding quantitative criteria for determining DSs plagued the reliability of the fragility functions and may partly explain the contradictive conclusions arrived by different researchers.

In this paper, we aim to improve the state of the art of developing fragility curves for masonry infill walls by critically examining the existing methods of determining DSs.

To this end, we conducted an experimental test on nine full-scale masonry infilled RC frames with a focus on the damage phenomena of the wall panels with various parameters. Aleatory uncertainty was considered by performing repeated tests on specimens of identical parameters. Based on the detailed records of the visual damage, three existing methods of determining DSs, namely the phenomena-based, skeleton curve-based and maximum crack width-based methods, were compared and critically reviewed in terms of the dispersions of fragility functions and the significance of brick types. The influences of plaster and the presence of openings on the fragility functions were also investigated.

In-plane cyclic loading tests

Specimens

Nine full-scale masonry infilled reinforced concrete (RC) frame specimens and a bare RC frame specimen were designed and constructed per the Chinese seismic code (GB 50011-2010 2010) to represent a single span of a typical multi-story classroom building in China. The dimensions, cross-sectional reinforcement and materials of the RC frames were identical for all the specimens (Figure 1). The RC columns were cast into a foundation beam of an 850×850 mm cross-section. C30 commercial concrete of a measured compressive strength of 13.6MPa was used for the RC frame. HRB400 rebars and HPB300 rebars were utilized for the longitudinal reinforcement and transverse reinforcement, respectively. The measured yield strengths of the ϕ20, ϕ22 and ϕ25 HRB400 rebars were 428MPa, 395MPa and 424MPa, respectively, and that of ϕ10 HPB300 rebars was 288MPa.

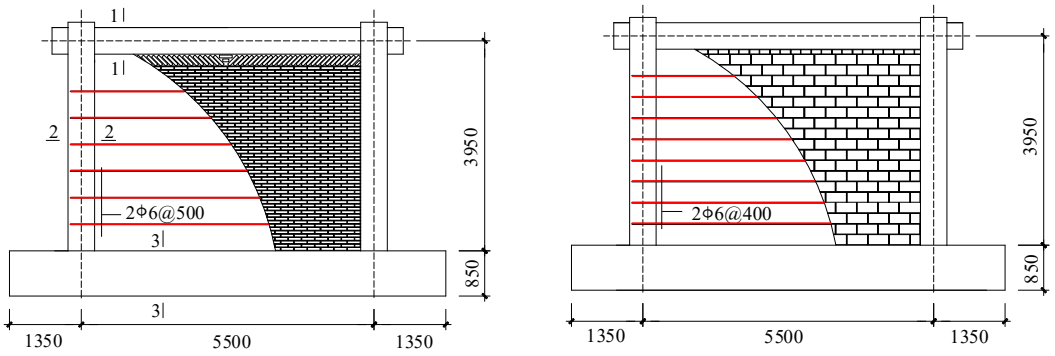

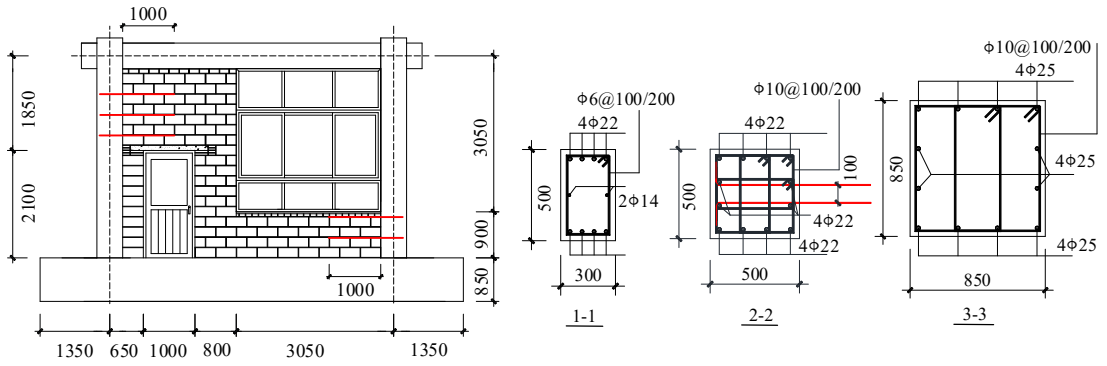

(c) (d)

Figure 1. Dimensions and reinforcement of specimens in (a) S group, (b) H group, (c) HO group and (d) cross-sections of RC frame members (unit: mm).

The infilled specimens fall into three groups, namely, the S group, H group and HO group, by the materials and configurations of the masonry. Three supposedly identical specimens exist in each group to assess the aleatory uncertainty, considering that FEMA P58 (2012) requires a minimum of three specimens of actual data to develop a fragility function of "moderate quality". In the S and H groups, the RC frames were fully infilled by solid clay bricks and hollow concrete blocks, respectively, to represent the spans in the transverse direction of the classroom building. In the HO group, the frame was infilled by hollow concrete blocks with large openings for a door and a window to represent a typical longitudinal span in the classroom building [Figure 1(c)]. For all specimens, the aspect ratio of the wall panels was 0.82, and the wall was laid after the RC frame was cured for more than 90 days.

The wall panels were constructed with a single wythe of 190 mm×190 mm×390 mm concrete hollow blocks (Figure 2) for the specimens in the H and HO groups and were constructed with 240 mm×115 mm×53 mm solid clay bricks for the S group specimens with a running bond. One surface of each wall panel was finished by 7-mm-thick plaster. Therefore, the nominal thickness of the wall panels was 197 mm for the H and HO groups and was 122 mm for the S group; the corresponding height-to-depth ratios were 18.8 and 30.3, respectively.

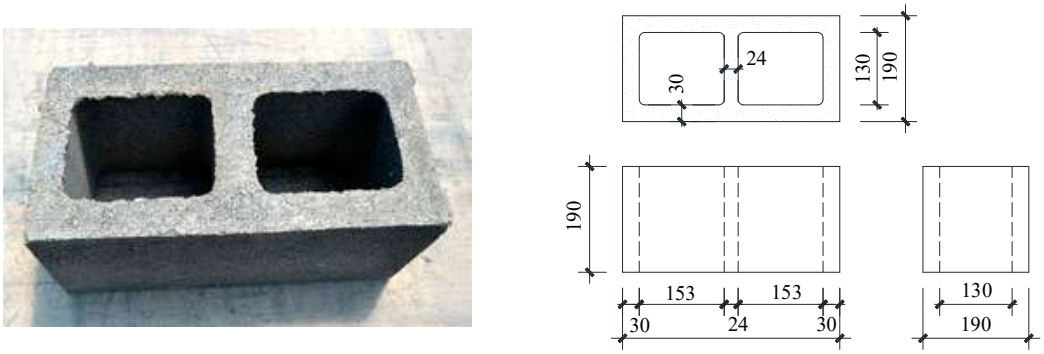

Figure 2. Hollow concrete block and its nominal dimensions. (unit: mm).

2ϕ6 tie bars were embedded along the mortar beds across the full span of the masonry infill walls at height-wise intervals of 500 mm and 400 mm for the specimens in the S and H groups, respectively, per the Chinese seismic code (GB 50011-2010 2010) [Figure 1(a) and (b)]. The tie bars were fastened to the longitudinal rebars in the RC columns before casting the concrete [Figure 1(d)]. For the specimens in the HO group, tie bars were placed along the mortar beds under the windows and above the doors at an interval of 400 mm, and extended into the mortar beds for 1 m [Figure 1(c)]. HPB300 rebars of 6-mm-diameter were used for the tie bars, and the measured yield strength and ultimate tensile strength are 405 MPa and 555 MPa, respectively.

The mortar of the masonry was mixed in the lab by lime, medium sand, water and cement by the mass proportion of 0.36: 5.27: 1.09: 1. The compressive strength of the mortar was tested on 70mm cubes and is listed in Table 1 for the three groups. The masonry compressive strength was tested on masonry prisms (Figure 3) per the Chinese standard (GB/T 50129-2011, 2011) for both the solid brick and hollow block masonry. The shear strength along the mortar bed was tested on coupons as shown in Figure 4 for both types of masonry. A pre-compression of 0.2 MPa was applied normal to the mortar bed to reduce the dispersion to a reasonable level (Dutu et al. 2015). Six coupons were tested for a single material property. The average strengths and coefficients of variance are summarized in Table 1.

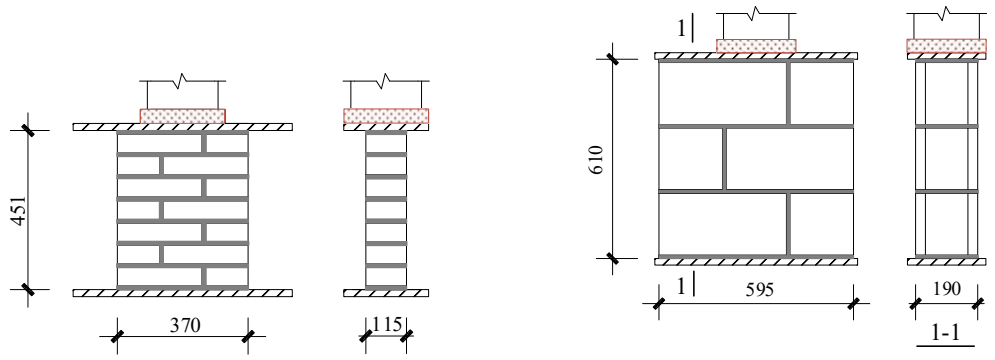

(a) (b)

Figure 3. Coupon dimensions and test setup for prism compressive strength of (a) solid clay brick masonry and (b) hollow concrete block masonry. (unit: mm).

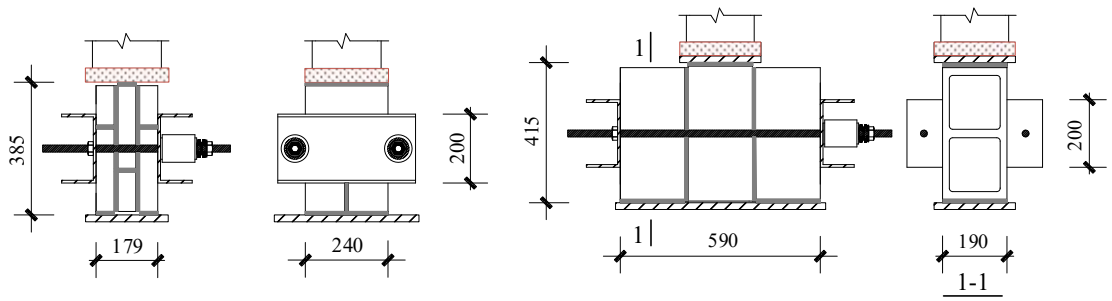

(a) (b)

Figure 4. Coupon dimensions and test setup for shear strength along mortar bed of (a) solid clay brick masonry and (b) hollow concrete block masonry. (unit: mm).

Table 1. Measured strengths of materials.

Specimen group	Compressive strength of mortar		Compressive strength of masonry		Shear strength of masonry*	
	Mean (MPa)	CV	Mean (MPa)	CV	Mean (MPa)	CV
H and HO	4.15	0.23	1.00	0.12	0.20	0.20
S	5.15	0.36	9.95	0.17	0.77	0.17

*Pre-compression of 0.2 MPa was applied normal to the mortar beds.

Test setup and measurements

The foundation beam of each specimen was firmly attached to the strong floor with 8 anchor bolts with a diameter of 70 mm. Two screw jacks were installed on both ends of the foundation beam to minimize sliding. A hydraulic jack with a capacity of 2000 kN was connected to the end of the RC beam via a steel jig to impose a cyclic lateral drift on the specimen. The jig was connected to another jig on the far end of the RC beam by two pairs of ϕ45 steel rods to ensure that the specimen could be pulled back when the hydraulic jack shrank. The two jigs were restrained by pantographs to eliminate the out-of-plane degrees of freedoms of the wall panel. Vertical loads other than the self-weight of the specimen were not applied to ensure a realistic stress condition of the infill walls, which are built after the primary structures are completed and are not supposed to carry any axial loads other than the self-weight. The lack of axial force may lead to smaller cracking and yield strengths of RC columns and have an influence on the deformation shape of the columns, especially those in the lower stories of a frame. These effects were not considered in the present test and because some frame-wall interaction is expected, the observed cracking pattern in frames with masonry infills may not represent that of frames with high axial loads on columns. The drawing and a photo of the test setup are provided in Figure 5.

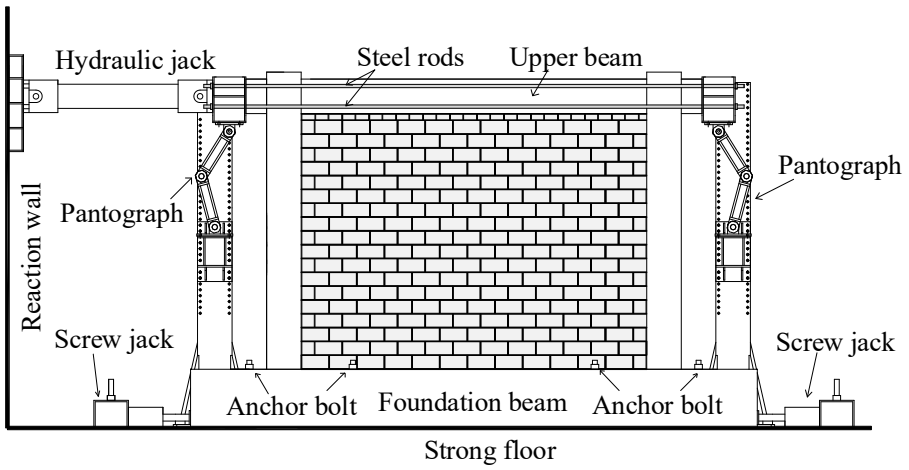

Figure 5. Loading setup.

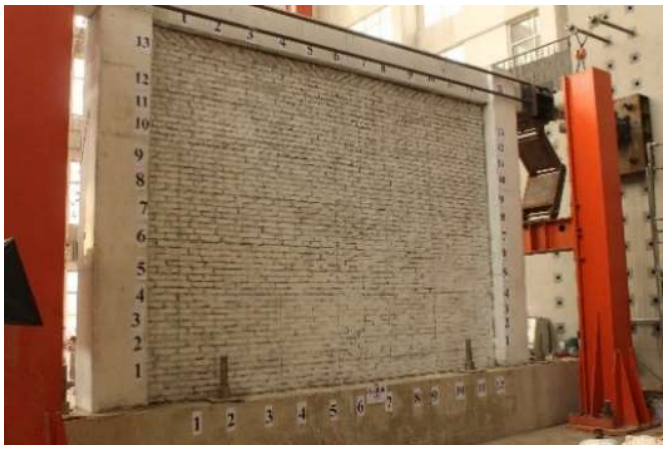

Figure 5. Loading setup (cont'd).

Because the primary purpose of the current test was to investigate the seismic fragility of the masonry infill walls and we intended to capture the onset of certain damage states as accurately as possible, a loading protocol of increasing the drift amplitudes by small steps was preferable to that by large steps. Therefore, the protocol suggested by FEMA 461 (2007) for determining the seismic performance characteristics of nonstructural components was employed. The quasi-static cyclic loading started from load cycles of a drift amplitude Δ_p=0.2 mm. The amplitude was increased by 1.19 times until Δ_p=84 mm (Figure 6). Two repeated load cycles were performed for each amplitude.

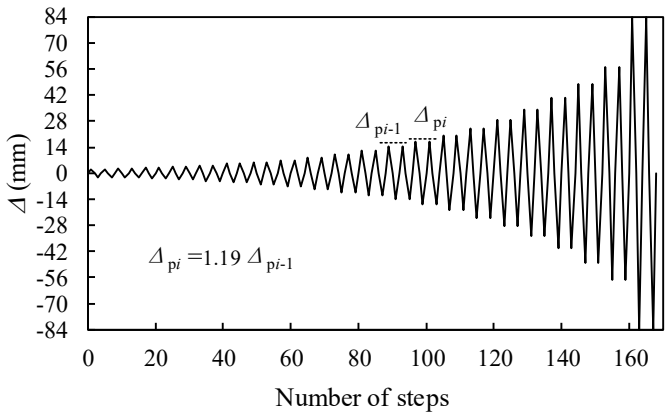

Figure 6. Loading protocol.

Four displacement sensors, Δ_1 to Δ_4, were installed to monitor the lateral drift Δ of the specimen (Figure 7). The story drift ratio R was calculated by Eq. 1 to remove the influence of the motion of the foundation beam, in which Δ_2 is the sliding of the foundation beam and $H(\Delta_3 - \Delta_4)/L'$ is the lateral drift due to rotation of the foundation beam. In addition to the displacement sensors, strain gauges were attached to the outermost longitudinal rebars at three sections (i.e., both ends and mid-length) of each beam and column of the RC frames. The locations of the sections are also depicted in Figure 7.

$$R = \left[\Delta_1 - \Delta_2 - \frac{H}{L'}(\Delta_3 - \Delta_4)\right]/H \quad (1)$$

where H=3950 mm is the distance between the top surface of the foundation beam and the axis of the frame RC beam; L'=7400 mm is the horizontal distance between Δ_3 and Δ_4 for the rotation of the foundation beam.

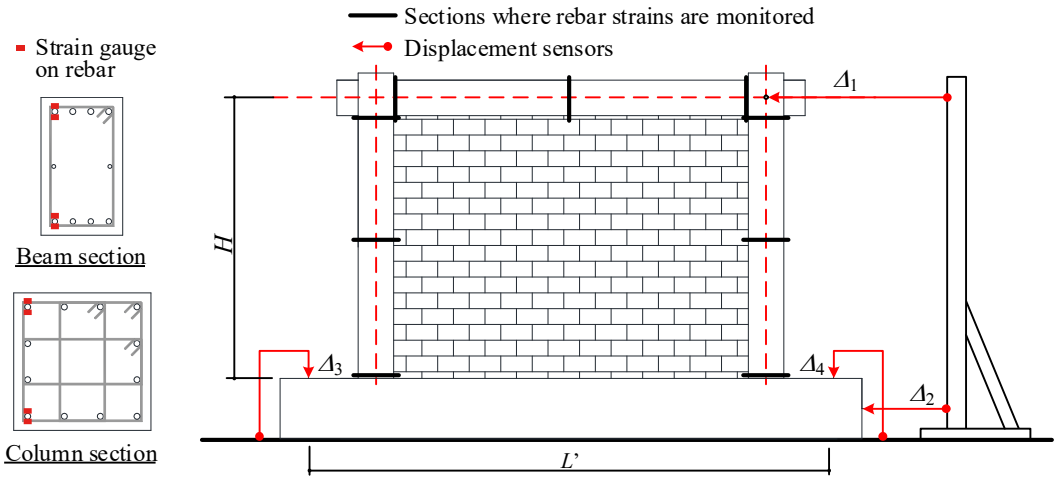

Figure 7. Displacement measurement.

Test results

Damage phenomena

For the specimens in the H group, slight shear cracks generally initiated from the mid-height of the masonry panels during the load cycles of the first two drift amplitudes of R=0.05% and R=0.06%. The maximum crack width did not reach 2 mm until R=0.11%, while the sliding gradually developed on the mortar beds. The major diagonal cracks continued to grow with significant sliding on the mortar beds as the story drift was increased, while new cracks were observed. The hollow blocks began to crush and some tie bars were exposed at R=0.52% for the three specimens in the group. The crushing became severer and some crushed concrete blocks fell as the lateral drift continued to increase.

For the specimens in the S group, light cracks appeared along the wall-column interfaces and in the corners of the wall panels during the first load cycle of R=0.05%. Diagonal cracks occurred on the wall panels before the drift reached 0.12%. The widths and number of cracks gradually increased as the lateral drift increased. The maximum widths of the major diagonal cracks were 2 mm at R=0.16% for the three specimens. Some cracks penetrated the bricks. Sliding on the mortar beds was also observed. The lateral drift ratios when the maximum crack width reached 4 mm for the three specimens varied from R=0.19% to R=0.22%. In the subsequent loading, significant sliding developed in the mortar beds, especially in those where the tie bars were embedded. The

plaster along the mortar beds gradually fell, and the tie bars were exposed. Some tie bars even buckled and bulged out of the wall at R=1%. Some bricks were crushed in the corners of the wall panels but no bricks fell during the test.

For the specimens in the HO group, cracks initiated at the corners of the windows during the first load cycles of R=0.05%. Light cracks were also observed along the interfaces between the masonry and the concrete lintels on top of the doors. Damage was concentrated in the narrow wall piers between the window and the door openings. The width of the main diagonal crack on the wall pier exceeded 2 mm at R=0.12% and exceeded 4 mm at R=0.21%. No part of the wall pier fell until R=0.28%. A large portion of the wall pier between the openings fell at R=2%.

The patterns and widths of the cracks on both sides of the masonry walls were carefully recorded at R=0.2% and R=0.52% in the test. The results are depicted in Figure 8. The specimens in both the H and S groups exhibited similar cracking patterns that were predominated by both diagonal shear cracks and horizontal sliding cracks along the mortar beds. The concentration of damage to the narrow wall piers of the masonry walls with large openings in the HO group is clearly illustrated in Figures 8(e) and (f). In addition, the crack distributions on the plaster surfaces correspond well to those on the bare masonry surfaces for all specimens, except that most cracks on the bare masonry surface developed along the mortar beds while the cracks on the plaster surface were not bounded by the mortar beds.

The maximum crack widths during the loading were recorded when the lateral drift reached the prescribed amplitude of each load cycle for all the specimens (Figure 9). The specimens in both the H and S groups exhibited similar relationships between the maximum crack widths and the lateral drift ratio R, regardless of the different brick types. The specimens with large openings also exhibited a similar trend of crack growth when the lateral drift ratio was less than 0.2%, beyond which the maximum crack widths grew with an increase in drift ratio much faster than those in the specimens without openings. The comparison between Figure 9(a) and (b) shows that the maximum crack width recorded on both the plaster and the bare masonry surfaces are similar.

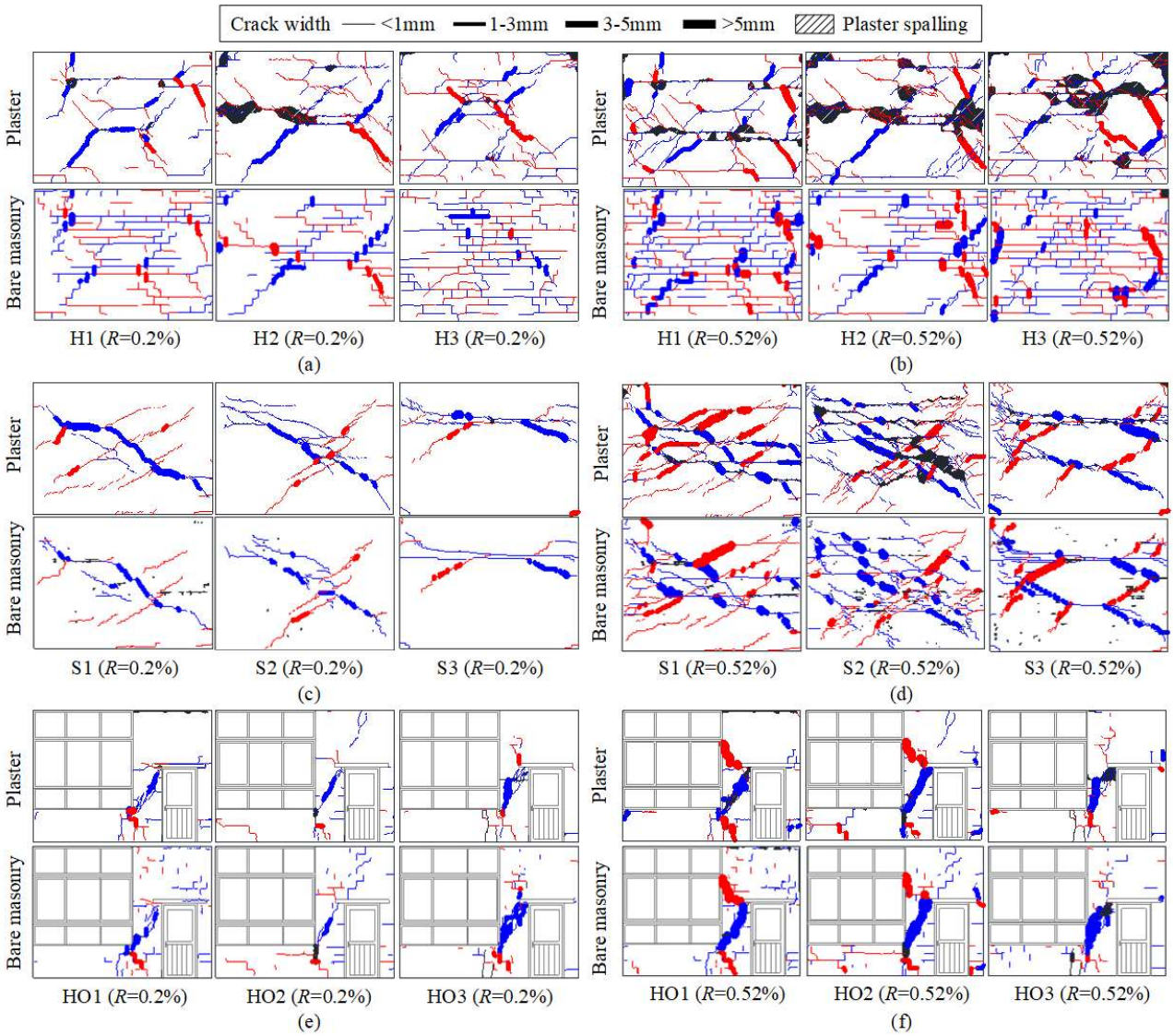

Figure 8. Crack patterns on both surfaces of wall panels of specimens in (a) H group at R=0.2%, (b) H group at R=0.52%, (c) S group at R=0.2%, (d) S group at R=0.52%, (e) HO group at R=0.2% and (f) HO group at R=0.52%.

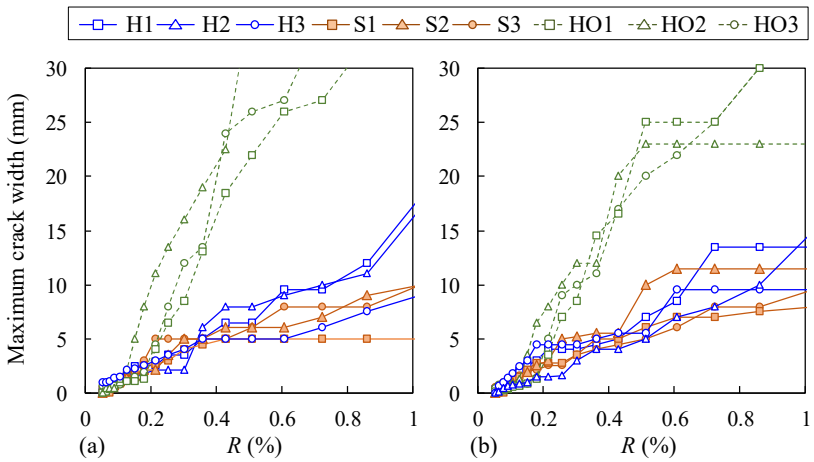

Figure 9. Maximum crack widths (a) on plaster surface and (b) on bare masonry surface.

Force-displacement curves

A separate bare frame specimen was tested by the same loading protocol as the masonry infilled frame specimens, which enabled an approximate extraction of the force-displacement hysteretic curves of the wall panel from the overall response of the infilled frame specimen. Individual loops of the hysteretic curves of the infilled specimen and bare frame specimen were linearly interpolated to be aligned with the same set of drift ratios at uniform small intervals. The subtraction of the hysteretic curve of the bare frame specimen from that of the infilled specimen gives the hysteretic curve of the masonry wall alone in the infilled specimen (Figure 10).

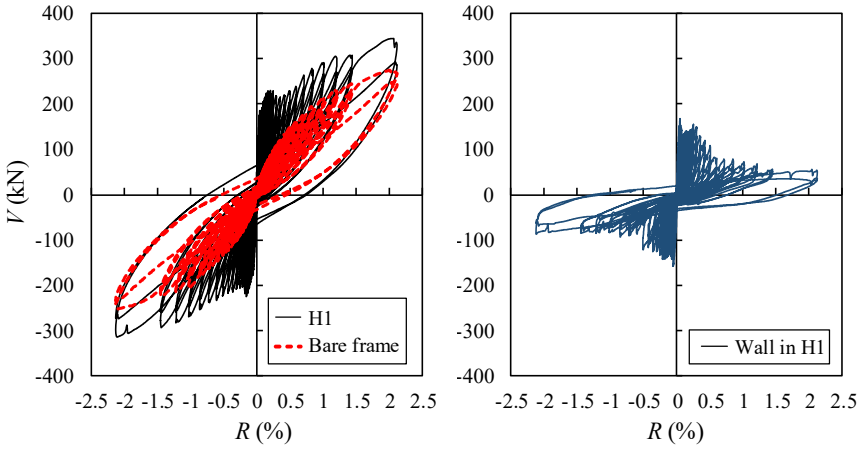

Figure 10. Extraction of hysteretic curve of wall panel from overall response of specimen H1.

The obtained hysteretic curves of all the infill walls were depicted in Figure 11. The specimens of hollow concrete block masonry reached the lateral strength at very small drift ratios and then sustained a rapid loss of strength until a remnant of approximately 30% strength was retained [Figure 11(a)-(c)]. The solid brick walls exhibited more than twice the strengths of the hollow block walls, and unlike the hollow block walls, the strength was retained without significant losses for a wide range of lateral drifts. In particular, the lateral force carried by the wall in specimen S2 continued to increase until a lateral drift ratio of R=1.2% was attained [Figure 11(d)-(f)]. The hollow block walls with large openings had very small lateral strengths, and similar to the full walls in the H group, rapidly lost their strength after they reached their peaks. However, the lateral load continued to increase when the frames of the windows and doors started to contribute a major part for the lateral resistance [Figure 11(g)-(l)]. Therefore, the hysteretic curves represented a combination of the lateral resistances of both the masonry wall and the frames of the window and the door.

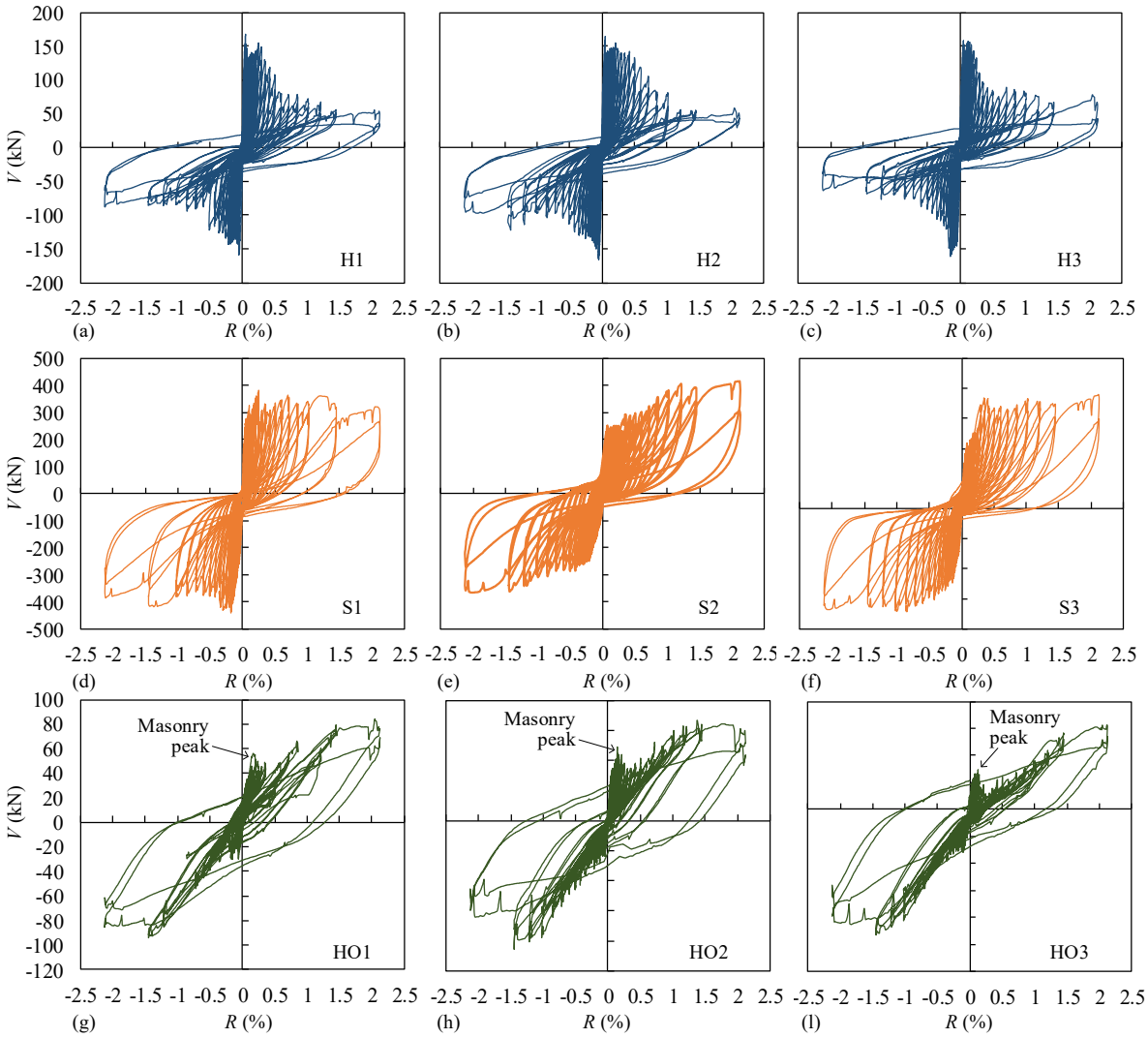

Figure 11. Hysteretic curves of infill walls in specimens: (a) H1, (b) H2, (c) H3, (d) S1, (e) S2, (f)S3, (g) HO1, (h) HO2 and (l) HO3.

These hysteretic curves extracted by the subtraction in Figure 10 were only approximate because the RC frames were not perfectly identical due to the scattering in material properties and workmanship despite that they were constructed by the same patch of materials and the same group of workers. More importantly, they were approximate because the masonry infills would have imposed large enough forces to significantly change the deformation patterns of the RC frames. The curvature distributions of the RC frames were derived from the strains of the longitudinal rebars at three cross sections of each beam and column to show this effect (Figure 12). For the H, S, and HO groups, the averaged curvature distributions of the three supposedly-identical specimens were depicted in the figure. While the curvature distributions of the bare frame were linear in the beam and the columns, those of the infilled frames were curved at the mid-length, suggesting a strong wall-frame interaction, especially for the specimens in the H and S series.

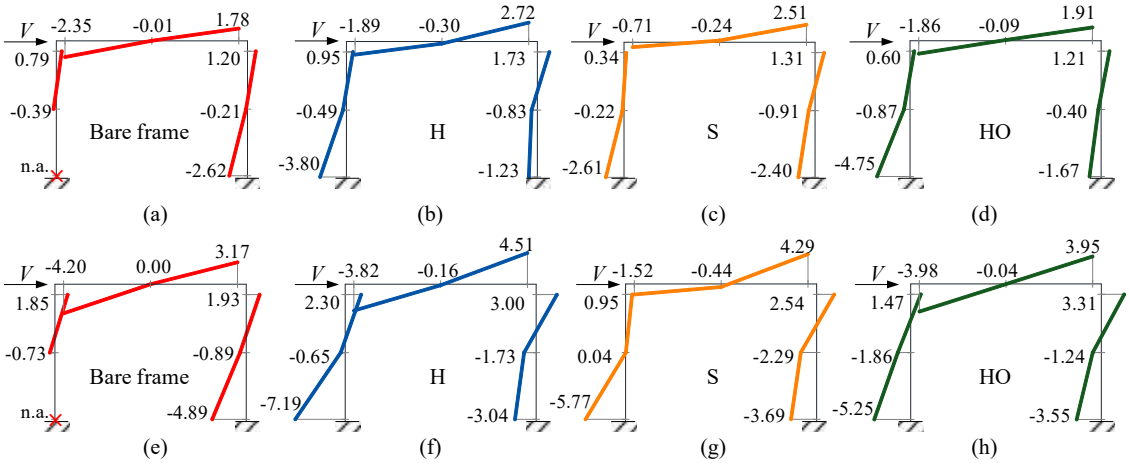

Figure 12. Curvature distributions of RC frames in: (a) bare frame specimen at R=0.2%, (b) H specimens at R=0.2%, (c) S specimens at R=0.2%, (d) HO specimens at R=0.2%, (e) bare frame specimen at R=0.52%, (f) H specimens at R=0.52%, (g) S specimens at R=0.52%, and (h) HO specimens at R=0.52%.

Damage states and their identification

For many nonstructural components, the damage states are defined by a quantitative damage measure, such as the ratio of falling panels of suspended ceilings (Badillo-Almaraz et al 2007), maximum sliding distance and rotation angles of free-standing contents (Konstantinidis and Nikfar 2015). These damage measures have distinct physical interpretations and correspond to well-defined consequences. They are quantifiable and objective to provide a common basis for comparing laboratory or field data from different sources and improving intensity measures for components of various parameters in the fragility analysis (Petrone et al. 2017).

The DSs of masonry walls have conventionally been defined by the onset of certain phenomena, such as the initiation of visible cracks, formation of significant cracks, spalling of plaster and crushing of bricks. These phenomena are familiar to practitioners and are strongly related to a certain set of repair methods. Chiozzi and Miranda (2017) adopted this kind of phenomena-based criteria in developing fragility functions of masonry infills based on a database of 152 collected specimens. The criteria and advisable repair efforts for each damage state are listed in Table 2. Similar criteria were adopted by Cardone and Perrone (2015) and Sassun et al. (2016). Although many tests of masonry infilled frames have been carried out by researchers over the globe, only a few reported detailed information about the visible damage to the infill walls, primarily because they were more focused on the behaviors of the structural members instead of the behaviors of the nonstructural walls (Cardone and Perrone 2015). Even if the damage phenomena were reported, the phenomena-based criteria for determining the onset of a DS could sometimes produce biased and subjective conclusions (Sassun et al. 2016).

Table 2. Consistent definitions of damage states (DS) by different criteria.

	Method 1 Phenomena-based criteria (Chiozzi and Miranda 2017)	Method 2 Force-displacement skeleton curve (Cardone and Perrone 2015)	Method 3 Maximum crack width (Cardone and Perrone 2015; Chiozzi and Miranda 2017)	Advisable repair effort (Chiozzi and Miranda 2017)
DS_1	Initiation of small hairline cracks in masonry, mainly concentrated in bed and head joints in plaster (when present) or along the interfaces with the columns and/or the top beam of the frame. No significant joint sliding and crushing of the units is observed.	2/3 peak strength	1 mm	Only very light and simple repair interventions, such as local plastering of visible cracks and application of new painting.
DS_2	Beginning of significant cracks, more than 2 mm wide, that propagate through both mortar joints and masonry blocks with possible but very limited sliding between joints and localized crushing of units (for example, at the corners).	Peak strength	2 mm	Removal of the old plaster, demolition of broken bricks, local reconstruction of masonry, application of a new higher-quality plaster coat and new painting.
DS_3	Development of wide diagonal cracks (usually larger than 4 mm) with significant sliding between joints and widespread crushing and spalling of masonry units.	20% strength loss	4 mm	Repair of the panel is not economically convenient. Complete demolition and subsequent reconstruction are advised.

As a remedy for either a lack of detailed information of visual damage or a biased and subjective judgment, Cardone and Perrone (2015) proposed to determine the drift at the onset of a DS on the force-displacement skeleton curve, which was usually available in the test results in the literature. They assumed that a DS of extensive cracking (DS_2) occurs at the peak strength point, that a damage state of light cracking (DS_1) occurs at 2/3 of the peak strength, and that the third DS may occur at 20% strength loss [Method 2 in Table 2]. This set of criteria were adopted by Sassun et al. (2016) to check the validity of the judgments of the phenomena-based criteria. Nevertheless, Chiozzi and Miranda (2017) did not employ this method and suggested that the procedure is not straightforward and can be misleading. They also pointed out a realistic difficulty that the force-displacement skeleton curves in the literature usually included the contribution of the surrounding frame, which was not easy to remove due to a lack of enough details. Even if the full details of the surrounding frame were available, which was the case in the present test in this paper, the removal of the RC frame contribution was approximate (Figure 12).

In the phenomena-based criteria adopted by both Chiozzi and Miranda (2017) and Cardone and Perrone (2015), a quantitative limit for crack width was usually suggested for a certain DS to help distinguish light cracks and significant cracks. Cardone and Perrone (2015) considered cracks with widths less than 1 mm as light cracks, whereas Chiozzi and Miranda (2017) considered a width of 2 mm as the threshold for a crack to be significant and considered the development of cracks wider than 4 mm as a sign of the onset of the third damage state. Such crack width-based criteria are listed in Table 2 as a third method of defining the DSs (Method 3). The crack widths of 1mm, 2mm and 4mm were adopted as the limit crack widths for DS_1, DS_2 and DS_3 so that the criteria in Method 3 represents a subset of the phenomena-based criteria in Method 1. This is to provide a basis for comparing the two methods later in the paper. These limit crack widths are by no means universally accepted to define visible, light, or significant cracks of masonry walls. For example, the Chinese national standard for the classification of earthquake damage to buildings (GB/T 24335-2009 2009) adopts 0.5mm, 1.5mm and 3.0mm for the limit widths of visible, slight and significant cracks of masonry walls, respectively. Despite the specific values of the limit crack widths, Method 3 is quantitative but may face the problem of lack of detailed data in the literature. The cons and pros of the three methods for defining the damage states are summarized in Table 3.

Table 3. Cons and pros of different methods of defining damage states.

Property	Method 1 Phenomena-based criteria (Chiozzi and Miranda 2017)	Method 2 Force-displacement skeleton curve (Cardone and Perrone 2015)	Method 3 Maximum crack width (Cardone and Perrone 2015; Chiozzi and Miranda 2017)
Quantitative	No	Yes	Yes
Data availability	Good	Poor	Poor
Correlation with consequences	Strong	Weak	Strong

The test results of this study included all information necessary for identifying the DSs by all the three methods. The lateral drift ratios at the onset of the three DSs by the phenomena-based criteria were identified from the visual observations and are listed in the 2nd to 4th columns in Table 4 for all the infilled specimens. Figure 13 shows photos of examples of hollow concrete and solid clay masonry walls when they were deemed to have reached DS_2 and DS_3.

Table 4. Lateral drift ratios at onset of damage states.

Specimen	Method 1 Phenomena			Method 2 Skeleton curve			Method 3 Maximum crack width		
	DS_1	DS_2	DS_3	DS_1	DS_2	DS_3	DS_1	DS_2	DS_3
H1(%)	0.053	0.127	0.510	0.035	0.053	0.543	0.053	0.123	0.303
H2(%)	0.063	0.090	0.510	0.036	0.053	0.087	0.109	0.139	0.322
H3(%)	0.063	0.090	0.510	0.035	0.053	0.274	0.107	0.202	0.331
S1(%)	0.127	0.214	0.857	0.051	0.255	0.300	0.090	0.154	0.197
S2(%)	0.090	0.180	0.608	0.338	1.218	-	0.113	0.167	0.303
S3(%)	0.090	0.180	0.723	0.169	0.361	-	0.102	0.174	0.271
HO1(%)	0.053	0.180	0.510	0.087	0.208	0.371	0.121	0.181	0.207
HO2(%)	0.053	0.180	0.429	0.052	0.151	0.231	0.107	0.189	0.214
HO3(%)	0.053	0.151	0.303	0.040	0.129	0.155	0.101	0.124	0.143
θ(%)	0.068	0.148	0.530	0.066	0.160	0.244	0.098	0.159	0.246
β_r	0.31	0.32	0.30	0.80	1.05	0.60	0.24	0.18	0.29
β	0.40	0.41	0.39	0.84	1.08	0.65	0.35	0.31	0.38

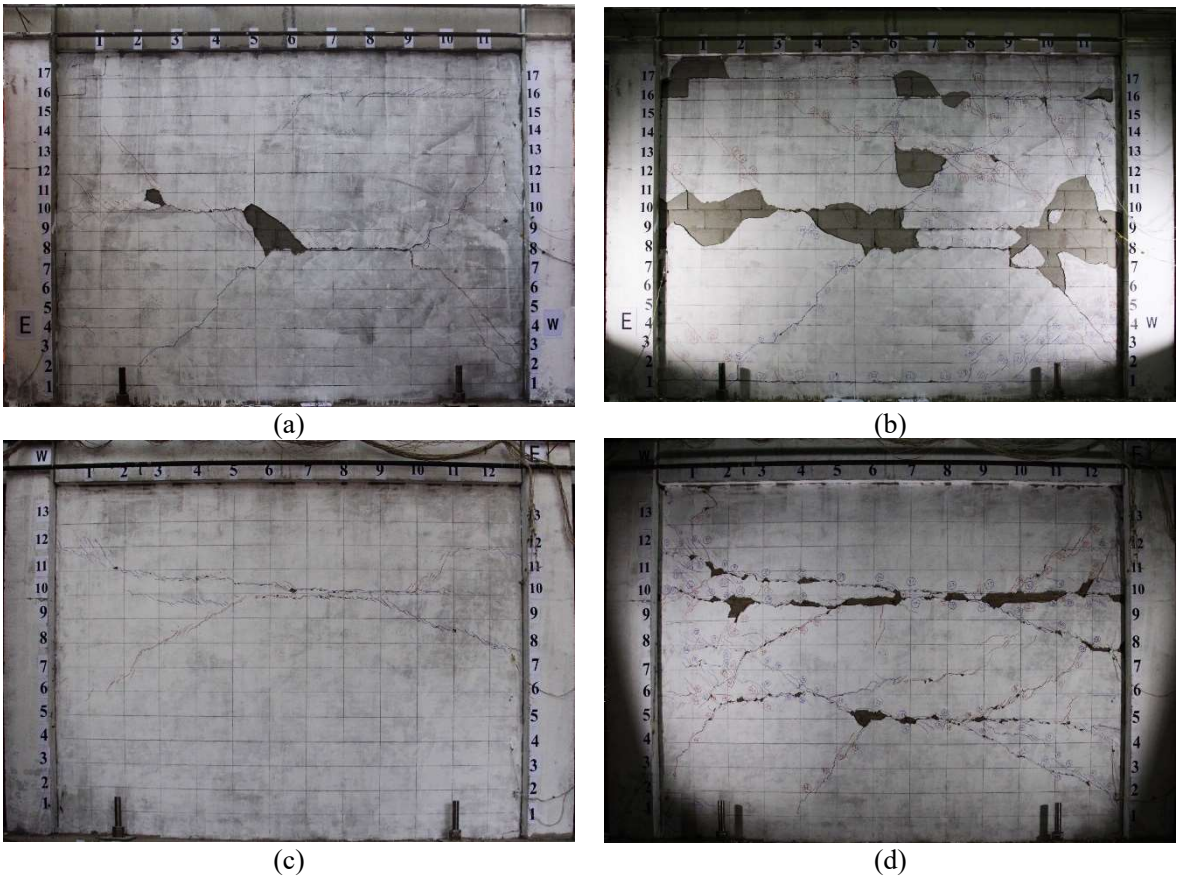

(a) (b) (c) (d)

Figure 13. Photos of plater surfaces of (a) H2 at DS_2, (b) H2 at DS_3, (c) S3 at DS_2 and (d) S3 at DS_3.

The logarithmic mean θ (Eq. 2) and standard deviation β_r (Eq. 3) are listed at the bottom of the columns in Table 4. β_r accounts for both the specimen-to-specimen variability of the sample with different mechanical and geometric parameters and the aleatory uncertainty due to the inherent randomness exhibited by repeated tests on supposedly identical specimens.

$$\theta=\exp\left[\frac{1}{N}\sum_{i=1}^{N}\ln R_{\mathrm{i}}\right] \quad (2)$$

$$\beta_{\mathrm{r}}=\sqrt{\frac{1}{N-1}\sum_{i=1}^{N}[\ln(R_{\mathrm{i}}/\theta)]^2} \quad (3)$$

where N is the number of specimens in the sample, and R_{i} is the lateral drift ratio at onset of a damage state of the i^{th} specimen.

The force-displacement skeleton curves in the positive loading direction of all the infill walls were extracted from their respective hysteretic curves and are depicted in Figure 14. The points that correspond to the three damage states defined by Method 2 in Table 2 are marked on the skeleton curves. For the solid brick masonry walls in specimen S2 and S3, the DS_3 could not be identified because the wall did not exhibit a minimum strength loss of 20%. For the specimens with large openings, the lateral force at the first peak in the hysteretic curve was considered the strength of the wall because the increased lateral force at larger drift ratios was attributed to the window and door. The lateral drift ratios that correspond to the damage states are listed in the 5th to 7th columns of Table 4. A significant difference as compared to the results obtained by Method 1 is the much greater β_{r}'s.

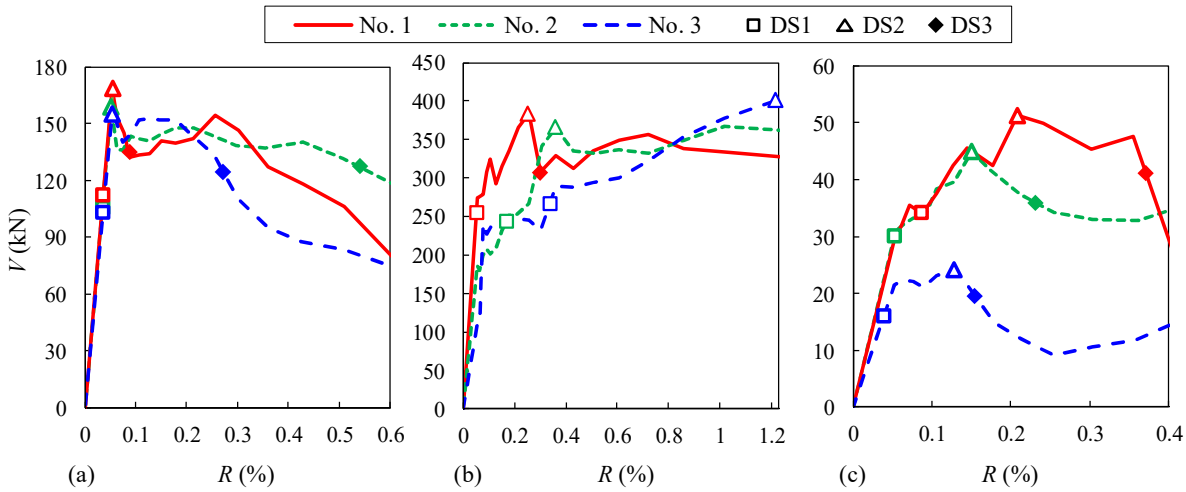

Figure 14. Force-displacement skeleton curves of specimens in (a) H group, (b) S group and (c) HO group.

The maximum crack width on the plaster surface is used to identify the damage states by Method 3. The relationships between the maximum crack width and the lateral drift ratio are depicted in Figure 15. The drift ratios when the curve reached maximum crack widths of 1mm, 2mm and 4mm were considered the drift ratios that correspond to the onset of DS_1, DS_2 and DS_3, respectively. These drift ratios are listed in the 8th to 9th columns of Table 4. While the logarithmic means are similar to those obtained by the other methods, Method 3 gives the smallest dispersions β for all the three DSs.

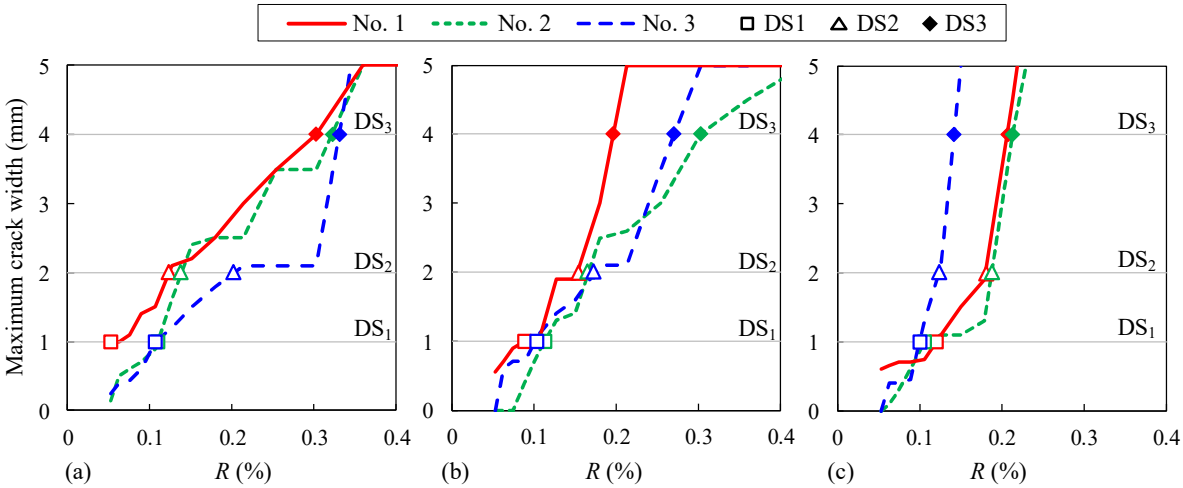

Figure 15. Maximum crack widths on plaster surfaces of specimens in (1) H group, (b) S group and (c) HO group.

Fragility functions

For a finite sample of experimentally obtained drift ratios at the onset of a specific DS, the probability of exceeding the DS is given in Eq. 4, which was proposed by Blom (1958).

$$P=\frac{j-3/8}{N+1/4} \tag{4}$$

where P is the probability of exceedance at the j^{th} smallest story drift ratio R_j in the sample, and N is the number of specimens in the sample. In this study, N=9 if all the infilled specimens are employed to form the sample.

The plot of the experimental drift ratios at the onset of a DS against the corresponding probability of exceedance calculated by Eq. 4 gives the empirical fragility function for the DS. The discrete empirical fragility function is usually fitted by an assumed cumulative probability distribution to obtain a continuous fragility function. The log-normal distribution is a common choice in engineering applications to build fragility functions for not only nonstructural components but also structural components (Petrone et al. 2017). Its probability distribution is fully defined by the logarithmic mean θ and standard deviation β_r as

$$P=\Phi\left[\frac{\ln(R/\theta)}{\beta_r}\right] \tag{5}$$

where P is the probability of exceeding a certain DS at the drift ratio R, and Φ is the cumulative standard normal distribution.

The empirical and fitted fragility functions based on the data in Table 4 are depicted in Figures 16 to 18 for the three DSs defined in Table 2 by three different methods. All the nine infilled specimens were included in the sample to account for the specimen-to-specimen variability, except for DS_3 by Method 2, for which only 7 specimens were included because the drift ratios that correspond to a 20% strength loss were not identified on the skeleton curves of two solid clay brick specimens. The Lilliefors tests (Lilliefors 1967) at 5% significance level were performed to confirm that all the fitted fragility functions passed the goodness-of-fit testing required by FEMA P-58 (2012).

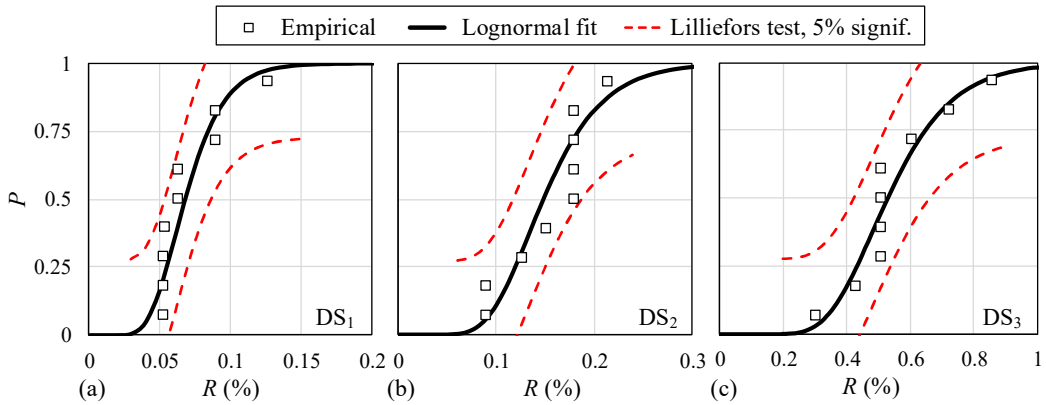

Figure 16. Fragility functions fitted to drift ratios obtained by phenomena-based criteria (Method 1) for damage state: (a) DS_1, (b) DS_2 and (c) DS_3.

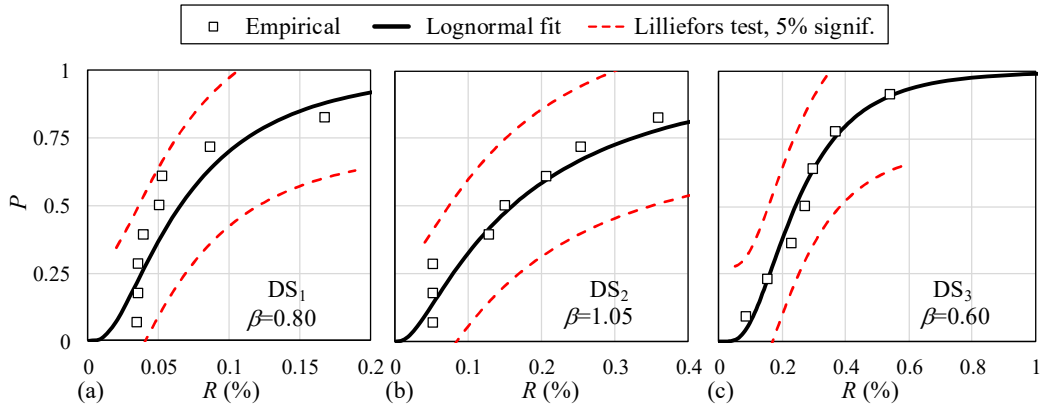

Figure 17. Fragility functions fitted to drift ratios obtained on skeleton curves (Method 2) for damage state: (a) DS_1, (b) DS_2 and (c) DS_3.

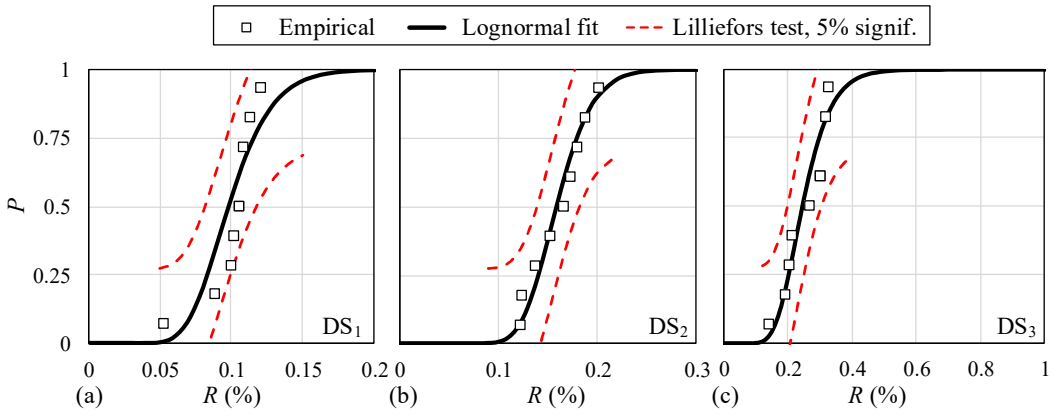

Figure 18. Fragility functions fitted to drift ratios obtained by maximum crack widths (Method 3) for damage state: (a) DS_1, (b) DS_2 and (c) DS_3.

FEMA P58 requires that an additional dispersion β_u is included for establishing the fragility function (FEMA P-58 2012). The overall dispersion β is expressed as the root of the squared sum of β_t and β_u (Eq. 6). The dispersions β for all the infill-specimens are listed at the bottom of Table 2 and β_u=0.25 as per FEMA P58, because the specimens were all subjected to the same loading protocol.

$$\beta = \sqrt{\beta_r^2 + \beta_u^2} \tag{6}$$

where β_u accounts for the uncertainty due to either a discrepancy from actual installation and loading conditions or inadequate sample size.

By replacing the β_r in Eq. 5 with the overall dispersion β gives Eq. 7 for the fragility function, the corresponding fragility curves for the three DSs defined by the three methods are compared in Figure 19.

$$P = \Phi\left[\frac{\ln(R/\theta)}{\beta}\right] \tag{7}$$

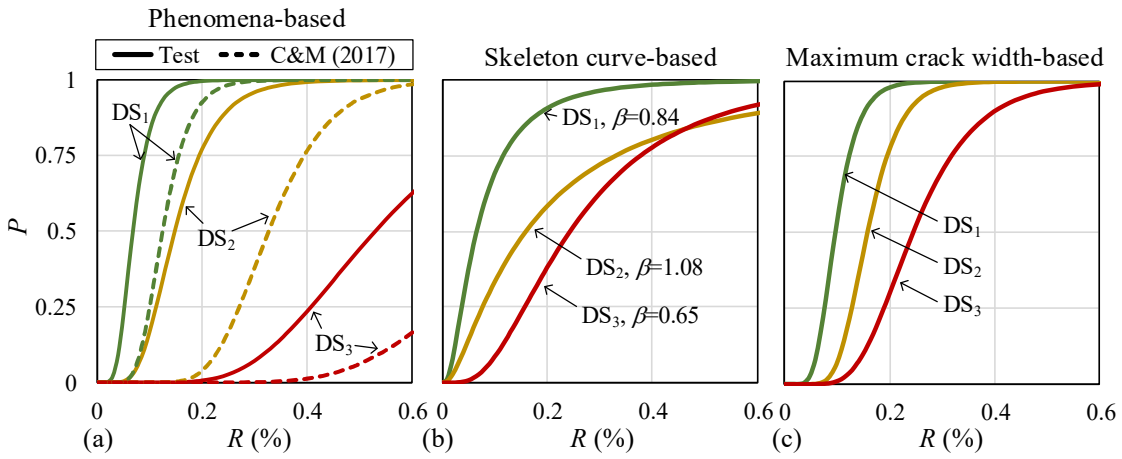

Figure 19. Fragility functions of masonry infill walls for damage states defined by (a) Method 1, (b) Method 2 and (c) Method 3 (C&M stands for Chiozzi and Miranda).

Although the fragility functions were derived from the same test, Method 2, which defines the damage states by the force-displacement skeleton curves, yields excessive dispersions compared with the other methods. The dispersions β for all the three DSs exceed the upper bound of 0.6 for the quality of the fragility function to be classified as high or moderate. In addition, the dispersion for DS_2 is much larger than that for DS_3, which causes an artificial crossing of fragility curves at R=0.46%. Also considering the ambiguous connection between the characteristic points on the skeleton curves and the actual extents of damage to the masonry walls, Method 2 should be avoided when developing fragility functions. In contrast, all the fragility functions by Methods 1 and 3 can be classified as "high quality" in terms of the number of specimens (≥5), dispersion (0.2-0.6) and whether it passes the Lilliefors test, according to the FEMA P58 criteria.

The fragility functions established by Chiozzi and Miranda (2017) are compared with those based on the present test in Figure 19(a). For all the three DSs, the fragility functions of Chiozzi and Miranda (2017) have much greater logarithmic mean θ and slightly smaller dispersions β (=0.325, 0.278 and 0.320 for DS_1, DS_2 and DS_3, respectively). Both sets of fragility functions were developed by the same method and the same definition of DSs (i.e. Method 1), but were based on different databases. The 152 specimens in the database of Chiozzi and Miranda (2017) were derived from 33 experimental programs conducted over the past several decades in Europe, US, Iran, Canada, China, India and New Zealand. They had dimensions ranging from full-scale to 1/4 scale, and were constructed with five types of bricks/blocks of a prism compressive strength ranging from 1.0 to 35.4MPa. Among them, 29 had openings of various configurations. The parameters of the nine specimens in the present test constituted only

a small subset of those of the large database. This is considered the primary reason for the significant difference in the logirthmic means of the fragility functions.

Influence of brick type and opening

The full sample was divided into three subsamples to investigate the influence of brick types and existence of openings on the fragility functions. Each subsample included three supposedly identical specimens of the H, S and HO groups subjected to the same loading protocols. Therefore, the specimen-to-specimen variability is supposed to diminish, leaving only aleatory uncertainty in each subsample. Independent two-sample *t*-tests were performed to determine if the means of two subsamples were significantly different. The subsample sizes were equal and the subsamples were assumed to have the same variance. The *t* statistic of the two subsamples was calculated by Eq. 8.

$$t=\frac{\mu_{\ln}^{(1)}-\mu_{\ln}^{(2)}}{s_{\mathrm{p}}\sqrt{\frac{1}{n_1}+\frac{1}{n_2}}} \tag{8}$$

where $\mu_{\ln}^{(k)}$ is the mean of the logarithms of the drift ratios ln$R$ in the k^{th} subsample; k=1 or 2; s_{p} is an estimate of the pooled standard deviation of the two subsamples and is calculated by Eq. 9; and n_1=n_2=3 is the subsample size.

$$s_{\mathrm{p}}=\sqrt{\frac{\sum_{i=1}^{n_1}\left(\ln\ _i-\mu_{\ln R}^{(1)}\right)^2+\sum_{i=1}^{n_2}\left(\ln\ _i-\mu_{\ln}^{(2)}\right)^2}{n_1+n_2-2}} \tag{9}$$

The statistic *t* represents the normalized difference between the means of the two subsamples; t=0 if the means are the same. The smaller *t* is, the more likely the null hypothesis that the two subsamples are not significantly different will be accepted. The probability of having a normalized difference between the means of two subsamples larger than $|t|$ or smaller than $-|t|$ can be obtained on an ordinary Student's *t*-distribution with the degree of freedom df=n_1+n_2-2. The null hypothesis must be rejected if the probability, denoted as $p_{\text{t-test}}$, is smaller or equal to a prescribed significance level, which is usually 5% in a significance test.

Figure 20 depicts the $p_{\text{t-test}}$ obtained by the *t*-test with the drift ratios for the three DSs of the subsample H versus subsample S and the three DSs of subsample H versus subsample HO. If Method 1 is utilized to determine the DSs, the null hypothesis must be rejected and the difference between the H and S subsamples is considered statistically significant for all the three DSs. In other words, the brick type has a significant influence on the fragility functions. However, the opposite conclusion that the brick type does not have a significant difference must be formed if Method 3, which is based on the quantitative maximum crack widths, is adopted to determine the DSs [Figure 20(a)]. Similarly, the drift ratios determined by Method 1 and Method 3 enable opposite conclusions regarding whether the existence of openings had a significant effect for DS_2 and DS_3 [Figure 20(b)].

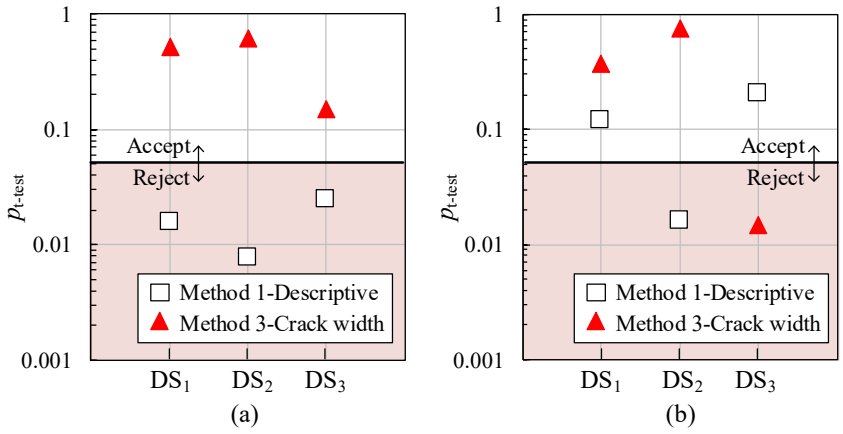

Figure 20. Probability $p_{t\text{-test}}$ in *t*-tests on subsamples of (a) H vs S and (b) H vs HO.

The phenomena-based criteria in Method 1 contain multiple phenomena of damage to determine if a specific DS occurs. Among the different phenomena, cracking is always an important concern, and the significance of a crack relies on the maximum crack width, which is the basis for Method 3. In this sense, Method 1 contains Method 3. Therefore, the contradictive results given by Method 1 and Method 3, as shown in Figure 20, suggests that the phenomena-based criteria are not self-consistent and may cause a polysemic interpretation of the damage states.

Figures 21 and 22 depict the fragility curves of the three subsamples of H, S and HO specimens by Method 1 and Method 3, respectively. β_u is not considered in these curves. The significant discrepancy between the mean drift ratios of the H and S groups by Method 1 does not exist in those by Method 3 for all the three DSs. In addition, the fragility functions for the HO group at DS_1 and DS_3 by Method 1 failed the Lilliefors tests and are denoted as "Bad fitting" in Figure 21.

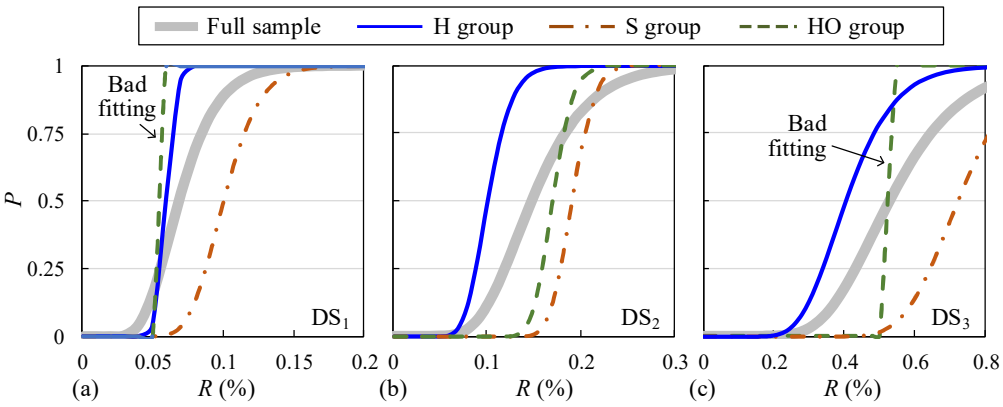

Figure 21. Fragility curves based on subsamples of drift ratios determined by Method 1 at damage state (a) DS_1, (b) DS_2 and (c) DS_3.

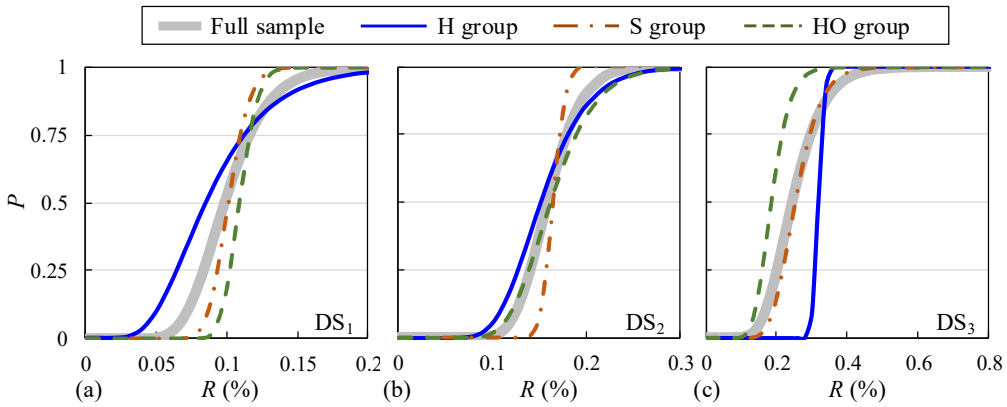

Figure 22. Fragility curves based on subsamples of drift ratios determined by Method 3 at damage state (a) DS_1, (b) DS_2 and (c) DS_3.

Influence of plaster

For all the nine infilled specimens, the maximum crack widths on both the plaster and the bare masonry surfaces were separately employed to determine two samples of drift ratios at the onset of the damage states. The *t*-test was performed on these two samples to check if the plaster had a significant effect in determining the DSs by Method 3. The null hypothesis was accepted for all the three damage states (Table 5). Therefore, the plaster is deemed to have no significant effect on the fragility functions by Method 3.

The fragility curves by Method 3 based on the maximum width of the cracks on the plaster and bare masonry surfaces are compared in Figure 23. The influence of plaster seems to diminish with the evolution of damage.

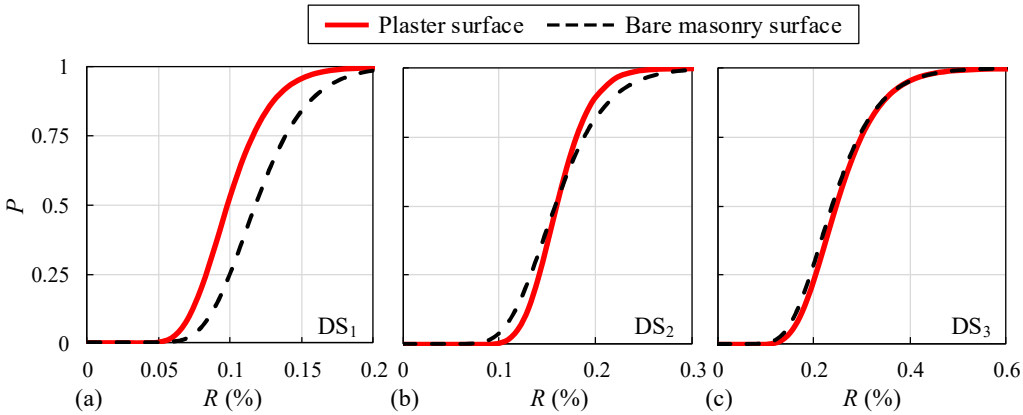

Figure 23. Fragility curves based on maximum width of cracks on plaster and bare masonry surfaces for (a) DS_1, (b) DS_2 and (c) DS_3.

Table 5. Probability $p_{t\text{-test}}$ for *t*-tests of significance of plaster.

t-test	DS_1	DS_2	DS_3
Plaster surface vs bare masonry surface	0.123 (Accept)	0.962 (Accept)	0.831 (Accept)

Conclusions

Based on the test results of nine full-scale masonry infilled RC frames that were subjected to in-plane cyclic loading, we investigated the damage characteristics of masonry infill

walls of solid clay bricks and hollow concrete blocks with or without openings. We carefully recorded the patterns and maximum widths of cracks on the wall panels during the tests and extracted the force-displacement hysteretic curves for the masonry walls by subtracting the curve of the bare frame specimen from that of the masonry infilled specimens. Based on the test results, three methods of defining the onset of damage states were critically reviewed by comparing the fragility functions based on each method. The influences of brick types, presence of openings and presence of plaster on the masonry surface on the fragility functions were investigated. The following conclusions can be drawn:

(1) The method of determining the onset of damage states by maximum crack widths is quantitative, feasible, and yielded the smallest dispersions compared with other methods based on either visible phenomena or force-displacement skeleton curves.
(2) The phenomena-based method was shown to be self-contradictory at all the three damage states in terms of the significance of brick types on the fragility functions. This was attributed to the polysemic interpretation of the damage states.
(3) Although quantitative, the method based on the force-displacement skeleton curves should be abandoned in developing fragility functions because it caused excessive dispersions, and the characteristic points on the skeleton curves were not shown to strongly correlate with the extents of visual damage to the masonry walls.
(4) The types of commonly employed bricks/blocks for masonry infill walls did not have a significant influence on the fragility functions of all the three damage states when the DSs were determined by the method based on the maximum crack widths. The presence of plaster did not have a significant effect on the maximum crack widths of the masonry walls.
(5) The presence of openings did not have a significant effect on the fragility functions of DS_1 and DS_2 but might have had a significant effect on DS_3 if the DSs were determined by the method based on the maximum crack widths.

Although its use for interpreting most existing data on masonry walls is difficult because of the lack of detailed records on crack widths, the method of defining the damage states based on the maximum crack width is considered to provide a quantitative basis for improving the reliability of fragility functions of masonry walls. With the fast development of photogrammetry and image processing technology, identifying, and measuring cracks will become much easier, which enables rapid accumulation of test data on the evolution of cracks on masonry walls. This improvement will help the understanding of the damage mechanism of masonry infill walls and increase the reliability of the fragility functions.

Funding

This work was supported by the Fund for Distinguished Young Scientists of the Heilongjiang Provincial Natural Science Foundation of China (JQ2019E005). This financial support is greatly appreciated.

References

Badillo-Almaraz, H., A. S. Whittaker, and A. M. Reinhorn. 2007. Seismic fragility of suspended ceiling systems. *Earthquake Spectra* 23 (1):21–40. doi: 10.1193/1.2357626.

Blom, G. 1958. *Statistical estimates and transformed beta-variables*. New York, NY: Wiley.

Calvi, G., D. Bolognini, and A. Penna. 2004. "Seismic performance of masonry-infilled RC frames: Benefits of slight reinforcement." In *Proceedings of 6th National Conference on Seismology and Earthquake Engineering*, 253–76. Guimaraes, Portugal: SISMICA.

Cardone, D., and G. Perrone. 2015. Developing fragility curves and loss functions for masonry infill walls. *Earthquakes and Structures* 9 (1):257–79. doi: 10.12989/eas.2015.9.1.257.

Chiozzi, A., and E. Miranda. 2017. Fragility functions for masonry infill walls with in-plane loading. *Earthquake Engineering & Structural Dynamics* 46 (15):2831–50. doi: 10.1002/eqe.2934.

Dutu, A., H. Sakata, Y. Yamazaki, and T. Shindo. 2016. In-plane behavior of timber frames with masonry infills under static cyclic loading. *Journal of Structural Engineering* 142 (2):04015140. doi: 10.1061/(ASCE)ST.1943-541X.0001405.

FEMA 461. 2007. *Interim testing protocols for determining the seismic performance characteristics of structural and nonstructural components*. Washington, DC: Federal Emergency Management Agency.

FEMA P-58. 2012. *Seismic performance assessment of buildings volume 1: Methodology*. Washington, DC: Federal Emergency Management Agency.

GB 50011-2010. 2010. *Code for seismic design of buildings*. Beijing: China Architecture & Building Press (in Chinese).

GB/T 24335-2009. 2009. *Classification of earthquake damage to buildings and special structures*. Beijing: Standards Press of China (in Chinese).

GB/T 50129-2011. 2011. *Standard for Test Method of Basic Mechanics Properties of Masonry.* Beijing: China Architecture & Building Press (in Chinese).

Holmes, W. T. 2000. "A vision for a complete performance-based earthquake engineering system." In *12th World Conference on Earthquake Engineering*. Auckland, New Zealand: WCEE.

Konstantinidis, D., and F. Nikfar. 2015. Seismic response of sliding equipment and contents in base-isolated buildings subjected to broadband ground motions. *Earthquake Engineering & Structural Dynamics* 44 (6):865–87. doi: 10.1002/eqe.2490.

Lilliefors, H. W. 1967. On the Kolmogorov-Smirnov test for normality with mean and variance unknown. *Journal of the American Statistical Association* 62 (318):399–402. doi: 10.2307/2283970.

Mainstone, R. 1971. "On the stiffnesses and strengths of infilled frames." In *Proceedings of the Institution of Civil Engineering, Supplement IV*, 57–90.

Mehrabi, A. B., P. B. Shing, M. P. Schuller, and J. L. Noland. 1996. Experimental evaluation of masonry-infilled RC frames. *Journal of Structural Engineering* 122 (3):228–37. doi: 10.1061/(ASCE)0733-9445(1996)122:3(228).

Negro, P., and A. Colombo. 1997. Irregularities induced by nonstructural masonry panels in framed buildings. *Engineering Structures* 19 (7):576–85. doi: 10.1016/S0141-0296(96)00115-0.

Paulay, T., and M. Priestley. 1992. *Seismic design of reinforced concrete and masonry buildings*. New York, NY: John Wiley & Sons, Inc.

Petrone, C., L. Di Sarno, G. Magliulo, and E. Cosenza. 2017. Numerical modelling and fragility assessment of typical freestanding building contents. *Bulletin of Earthquake Engineering* 15 (4):1609–33. doi: 10.1007/s10518-016-0034-1.

Porter, K., R. Kennedy, and R. Bachman. 2007. Creating fragility functions for performance-based earthquake engineering. *Earthquake Spectra* 23 (2):471–89. doi: 10.1193/1.2720892.

Pujol, S., A. Benavant-Climent, M. Rodriguez, and J. Smith-Pardo. 2008. "Masonry infill walls: An effective alternative for seismic strengthening of low-rise reinforced concrete building structures." In *Proceedings of the 14th World Conference on Earthquake Engineering*. Beijing, China: WCEE.

Sassun, K., T. Sullivan, P. Morandi, and D. Cardone. 2016. Characterising the in-plane seismic performance of infill masonry. *Bulletin of the New Zealand Society for Earthquake Engineering* 49:100–17. doi: 10.5459/bnzsee.49.1.98-115.

Taghavi, S., and E. Miranda. 2003. Response assessment of nonstructural building elements. Report No 2003/05. Berkeley: Pacific Earthquake Engineering Research Center.

Verderame, G. M., F. De Luca, P. Ricci, and G. Manfredi. 2011. Preliminary analysis of a soft-storey mechanism after the 2009 L'Aquila earthquake. *Earthquake Engineering & Structural Dynamics* 40 (8):925–44. doi: 10.1002/eqe.1069.

Yan, P., B. Sun, and H. Zhang. 2014. Seismic damage to RC frame teaching buildings in Lushan MS7.0 earthquake. *China Civil Engineering Journal* 47:24–8 (in Chinese).